

## Upgrade of a commercial four-probe scanning tunneling microscopy system

Ruisong Ma,<sup>1</sup> Qing Huan,<sup>1,2,a)</sup> Liangmei Wu,<sup>1</sup> Jiahao Yan,<sup>1</sup> Qiang Zou,<sup>1</sup> Aiwei Wang,<sup>1</sup> Christian A. Bobisch,<sup>3</sup> Lihong Bao,<sup>1</sup> and Hong-Jun Gao<sup>1,2</sup>

<sup>1</sup>*Institute of Physics, Chinese Academy of Sciences, P.O. Box 603, Beijing 100190, China*

<sup>2</sup>*School of Physics, University of Chinese Academy of Sciences, Beijing 100049, China*

<sup>3</sup>*Faculty of Physics, University of Duisburg-Essen, Duisburg 47057, Germany*

(Received 9 December 2016; accepted 3 June 2017; published online 19 June 2017)

Upgrade of a commercial ultra-high vacuum four-probe scanning tunneling microscopy system for atomic resolution capability and thermal stability is reported. To improve the mechanical and thermal performance of the system, we introduced extra vibration isolation, magnetic damping, and double thermal shielding, and we redesigned the scanning structure and thermal links. The success of the upgrade is characterized by its atomically resolved imaging, steady cooling down cycles with high efficiency, and standard transport measurement capability. Our design may provide a feasible way for the upgrade of similar commercial systems. *Published by AIP Publishing.* [<http://dx.doi.org/10.1063/1.4986466>]

### I. INTRODUCTION

The invention of scanning tunneling microscopy (STM) by Binnig and Rohrer<sup>1,2</sup> in the early 1980s provided mankind an extremely powerful tool to study and manipulate microscale systems down to sub-nanometer scale. Based on the principle of STM, various new techniques with high spatial resolution have been developed, such as atomic force microscopy (AFM),<sup>3</sup> ballistic electron emission microscopy (BEEM),<sup>4</sup> scanning tunneling potentiometry (STP),<sup>5–9</sup> scanning chemical potential microscopy (SCPM),<sup>10</sup> scanning thermopower microscopy (STPM),<sup>11,12</sup> spin-polarized STM,<sup>13,14</sup> and scanning near-field optical microscopy (SNOM).<sup>15,16</sup> They collectively belong to the scanning probe microscopy (SPM) family. However, initially STM/SPM systems had only one probe, and this single-probe (1-P) configuration limited its application in measuring the lateral electrical conductivity of nanostructures,<sup>17,18</sup> such as nanowires and 2D materials. In order to fully utilize the ultra-high spatial resolution of STM in traditional transport measurements, multi-probe SPM systems have emerged, with double probes,<sup>19–21</sup> triple probes,<sup>22,23</sup> or even four probes.<sup>24–30</sup>

Among these, the four-probe (4-P) STM is ideal for combining the ultra-high spatial resolution of STM with standard four probe transport measurements *in situ*.<sup>24,31–33</sup> To enable this capability, the 4-P STM has several special configurations compared to 1-P STM. First of all, for rough probe positioning, the 4-P STM system is usually combined with another imaging instrument, such as a scanning electron microscope (SEM).<sup>24,27,30,34</sup> In addition, in 1-P STM, the probe is normal to the sample surface, while in 4-P STM systems, the four probes are slanted relative to the normal of the sample surface,<sup>26–28,30,34</sup> which is essential for bringing the very ends of the probes as close as possible. Since four independent coarse motion motors and scanner tubes are integrated, the scanner of a 4-P STM system is usually larger than that of the 1-P

STM in size and mass, and the increased complexity in the 4-P STM system entails a cost in performance,<sup>26,27,30,34</sup> such as poorer resolution, higher base temperature, and lower cooling efficiency. Finally, for grounding or biasing, in the 4-P STM, all the probes share the same sample, so it is desirable to ground the sample and bias the probes individually, while in 1-P STM, both the biased sample (grounded probe) and biased probe (grounded sample) are accepted, with the former being more common.

Despite the differences and drawbacks mentioned above, the 4-P STM system possesses its own unique advantages. As is well known, the four-point method can eliminate ambiguity from the wire resistance and contact resistance in transport measurements. Moreover, compared to the traditional four-terminal method used in device testing, the probes in the 4-P STM system possess the freedom of moving in XYZ directions with high positioning precision, down to the sub-nanometer range. Benefitting from this, transport properties of nanowires,<sup>33,35,36</sup> quasi-one-dimensional structures,<sup>31,37,38</sup> 2D materials,<sup>39–43</sup> and surface state of three-dimensional materials<sup>32,44–46</sup> have been extensively studied. With the cooperation of all four probes driven by coarse motion motors and precision scanner tubes, transport measurement under different stresses can be performed on nanowires<sup>35</sup> and 2D materials like graphene.<sup>39,47</sup> In addition, the anisotropy of the surface structure and surface conductance can be directly measured either in a collinear or square configuration.<sup>31,41</sup> Surface and step conductivities on Si(111) surfaces can also be extracted via anisotropy measurement by a 4-P STM system.<sup>48</sup> Equipped with special electrical circuits, a multiple-probe SPM system can be extended to perform STP<sup>5–9</sup> and BEEM.<sup>4,49,50</sup> The development of multiple-probe STM and such systems' outstanding performance have been recently reviewed by Nakayama *et al.*<sup>17</sup> and Li *et al.*<sup>18</sup>

The 4-P STM system we have is one of the earliest commercially available systems of this kind. It is equipped with four independent STM probes inside an ultra-high vacuum (UHV) chamber along with an SEM mounted on top.

<sup>a)</sup> Author to whom correspondence should be addressed: [huanq@iphy.ac.cn](mailto:huanq@iphy.ac.cn)

In past years, we have carried out quite a number of experiments<sup>25,35,40,42,43,47,51</sup> on the system; however, our research is greatly restricted by its shortcomings in terms of noise, stability, and lowest temperature. The noise and drift during scanning were so big that we could barely get atomic resolution. Moreover, the lowest temperature ever reached was 130 K when cooling with liquid nitrogen (LN<sub>2</sub>).<sup>40,42,43</sup> Consequently, being a prototype, this commercial system cannot fulfill our objective to locate atomic-scaled structures from macroscopic scale quickly and accurately, and to position the four probes as close as possible and carry out transport measurements simultaneously. Furthermore, larger scanning range and higher piezo tube sensitivity/spatial resolution cannot be realized in a compatible way. In addition, novel properties at much lower temperatures cannot be revealed in transport measurements and scanning tunneling spectroscopy by this relatively primitive system.

According to our experience with this equipment, these deficiencies in the commercial design originate from three factors: the vibration isolation and damping design, the scanning structure, and the thermal links and thermal shielding.

- (1) In the original design, only two types of vibration isolation and damping mechanisms were employed: four air springs supporting the bench frame and Viton O-rings sandwiched between metal plates. This configuration has turned out to be insufficient for atomically resolved imaging.
- (2) Only the sample stage was connected to the cold finger of the cryostat through a bundle of copper braids, while the probes and other parts were kept at room temperature. In this way, the cooled sample was exposed to room-temperature surroundings, and there was a big thermal gradient between the probes and the sample when the system was running at reduced temperature. As a result, dramatic thermal drift and instability were presented, and the sample temperature never reached its expected lowest value.
- (3) The system has four scanner tubes, which are ~13 mm in diameter and ~28 mm in length. These scanner tubes, which are relatively bigger than normal STM scanner tubes, ensure a larger scanning range but sacrifice resolution. In order to bring all probes as close as possible, four long cantilevers are clamped on the scanner tubes, which hold the probes ~45° to the sample surface. This structure with a long cantilever possesses relatively low resonance frequency and couples easily with external vibrations. Therefore, getting high-resolution images has been very challenging.

In this paper, we report on upgrading the 4-P STM system for the three factors mentioned above. The success of this upgrade has been verified by atomically resolved imaging, steady cooling down cycles with high efficiency, and standard transport measurements.

## II. SYSTEM OVERVIEW

The commercial 4-P STM system (Omicron UHV Nanoprobe) is composed of two chambers: a main chamber

and a load-lock chamber. A long wobble stick and a carousel with 10 docking positions for sample holders and probe holders are mounted on the load-lock chamber. The long wobble stick is used to transfer probes and samples between the carousel in the load-lock chamber and another identical carousel in the main chamber. In order to pretreat samples *in situ*, a custom-designed annealing stage is integrated in the load-lock chamber, which can be heated resistively up to 550 °C.

Both chambers are fixed on a bench frame which is supported by four pneumatic air legs. A continuous-flow cryostat is mounted on the bottom flange (CF300) of the main chamber and is thermally linked to the sample stage through a bundle of copper braids. The reduced temperature at the sample stage can be obtained by pumping LN<sub>2</sub> or liquid helium (LHe) with a rotary pump. A solid-state resistive heating element is integrated in the sample stage for heating up to 500 K or counter-heating during cooling. The sample temperature is measured by a Pt 100 resistor fixed at the sample stage and is monitored and controlled by a Lake Shore 331 temperature controller. The temperature at the cryostat cold finger is measured by a Si diode connected to the second channel of the same temperature controller. Stacked stainless steel (SS) plates spaced with Viton O-rings were fixed on the bottom flange and were used as the supporting foundation for the four independent scanning units and the sample stage. All four original scanning units were identical which were composed of an XYZ coarse motion actuator, a piezo tube, and a probe holder with a long cantilever. The probe holders were attached on the scanner tubes through magnetic force to guarantee reliable mechanical and electrical contacts. All four probes are oriented at approximately 45° with reference to the sample surface, located at the center of the metal plate. An SEM (BDS-50, FEI Company, working distance: 15 mm–75 mm, 20 nm resolution at 25 mm working distance) was mounted on the top flange of the main chamber and was used for positioning probes with reference to the sample surface. Two short wobble sticks, which are mounted on the two sides of the main chamber, are used for sample and probe exchanging.

The system has a base pressure of around  $1 \times 10^{-10}$  Torr maintained by an ion getter pump and a titanium sublimation pump (TSP). The control electronics is composed of a SPM controller (OMICRON SCALA) and 4-channel high voltage (HV) amplifiers. Each probe could be driven either by the SPM controller when scanning on the surface (scanning mode) or by a HV amplifier when taking transport measurements (measuring mode). The currents from probes could be fed either into a current preamplifier or into a Keithley 4200 parameter analyzer depending on the work mode. An additional gate voltage could be applied by a Keithley 6430 source meter to tune the carrier density of studied materials during the electrical transport measurement. After upgrading the system, we replaced the SEM with a view port on the same flange that once supported the SEM. An optical microscope (Questar QM 100) with a long working distance ranging from 15 cm to 35 cm is used to monitor the probes and sample. The best resolution is 1.1 μm at 15 cm. The optical microscope (OM) is attached to a mobile support, which is isolated from the frame bench. The relative distance between the sample stage and the lens of the OM in XYZ directions can be adjusted and the optical axis can

be aligned with the normal of sample surface by twisting the rotary knobs in this rigid support. A computer-controlled CCD camera installed in the axial port of OM is used to position and quickly image the sample surface and probes.

### III. THE UPGRADING PROCESS

In order to improve the performance of our 4-P STM system, a detailed plan was proposed on account of its weaknesses mentioned in Sec. I. The upgrade mainly covers four aspects: the vibration isolation and damping, scanning structure, thermal links and thermal shielding, and replacement of the SEM by an OM. In this section, we will describe the upgrading in detail.

#### A. Vibration isolation and damping

The ultimate spatial resolution of STM comes from the exponential dependence of the tunneling current on the gap distance and its spatial confinement, which also makes STM extremely sensitive to external vibrations. Therefore, vibration isolation and damping play important roles in imaging capability. Good anti-vibration or anti-shock performance is of fundamental importance not only in STM characterization but also in electrical measurement, during which stable probe/surface contacts are required over a certain period of time.<sup>34</sup>

The original system employed four pneumatic air legs under the massive bench frame and a few layers of Viton rubber (O-rings) sandwiched between metal plates for vibration isolation and damping, as shown in Fig. 1(a). The pneumatic springs possess a resonance frequency as low as 0.5 Hz

and are widely used in many vibration-sensitive instruments. Rubber is a great material for springs and viscous damping since it is most effective against large amplitude shock and is substantially incompressible. By virtue of the high compressive stiffness, the resonance frequency of rubber typically lies between 10 Hz and 100 Hz.<sup>52</sup> Viton, a kind of UHV compatible rubber material, is widely used as a high-frequency isolator in some STM systems.<sup>53</sup> Reasonable isolation and damping has been achieved solely by a stack of metal plates with pieces of Viton O-rings sandwiched in between<sup>54</sup> or further cooperating with a pneumatic system.<sup>4,53</sup> This configuration is compact and ensures a fixed distance between the sample surface and the SEM electron gun, which simplifies focus adjustment. However, the actual performance of this commercial 4-P STM turned out to be insufficient for atomic resolution imaging and stable electrical contact.

In our new design, we added suspension springs and efficient eddy-current damping on the whole STM stage, as schematically shown in Fig. 1(b). Four suspended springs (blue parts) with an outer diameter of 10 mm, which are made of the 316 SS wire (1 mm in diameter) after proper thermal treatment, suspend the whole STM stage. The resonance frequency  $f_0$  of a linear spring supporting an object against the gravity depends only on the extension length  $L$  of the spring. This relationship is given by<sup>55</sup>

$$f_0 = \frac{1}{2\pi} \left( \frac{g}{L} \right)^{\frac{1}{2}}. \quad (1)$$

Under full load of the whole STM stage (roughly 6.8 kg), the resonance of these springs is approximately 2.73 Hz with an extension of 33.3 mm. Although metal springs can yield low resonance frequencies, they provide limited damping, so we

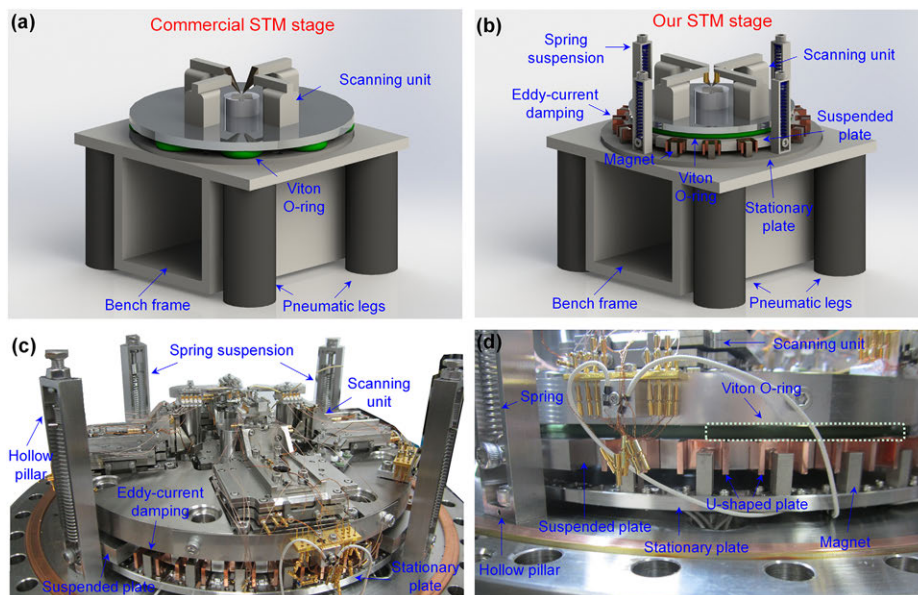


FIG. 1. Upgrade of the vibration isolation system. Schematic of the vibration isolation systems for the four-probe STM before (a) and after (b) upgrading. In the commercial damping design shown in (a), four pneumatic air springs hold the bench frame and several Viton O-rings are sandwiched between metal plates. In our design illustrated in (b), suspension springs and efficient eddy current dampers are supplemented to avoid vibration of the STM stage. A new Viton O-ring is sandwiched between the suspended plate and the plate holding the four scanning units. The relative distances and sizes of these parts are not to scale. [(c) and (d)] Digital photographs of the renewed vibration isolation systems. The suspension springs and eddy current dampers are shown in (c). The four hollow pillars hook the suspended springs and limit the motion of the suspended plates, compensating for the lack of a docking system. The Viton O-ring indicated by the dotted line in (d) is squeezed between the suspended plate holding the U-shaped copper plates and the plate holding the scanning units.

require an additional damping mechanism. We chose magnetic eddy current damping due to its vacuum compatibility and the ease of adjusting the damping coefficient.<sup>52</sup> In our design, we embedded 24 SmCo magnets (cuboid,  $15 \times 7.8 \times 5 \text{ mm}^3$ , magnetization direction: along the short side, Br:  $\sim 11 \text{ kGs}$ ) onto a round stationary plate which is fastened to the bottom flange. U-shaped oxygen-free high-conductivity (OFHC) copper plates [red parts in Fig. 1(b)] are fixed on the lowest suspended SS plate and alternately placed between magnets. The magnetic field will penetrate perpendicularly into the parallel surfaces of the U-shaped copper plates. The induced eddy current impedes the relative motion between the suspended parts and the stationary plate. A Viton O-ring (212 mm in ring diameter and 6.3 mm in wire diameter, dark green part) is sandwiched between the plate that supports all four scanning units and the lowest suspended SS plate, as can be seen in Fig. 1(b). The scanning unit has also been modified, as can be seen in Figs. 1(a) and 1(b), which will be introduced in detail in Sec. III C. Figures 1(c) and 1(d) are photographs of the upgraded vibration isolation system (pneumatic air legs are not included). We did not introduce any docking mechanism in the new design because of the space limitation. Instead, we designed hollow pillars to hook the springs which also restrict lateral motion of the suspended structures and minimize the risk of damaging fragile parts. Taking advantage of this design and of the heavy mass of the whole suspended part, we are able to change the sample and probes *in situ* without a docking mechanism.

## B. Thermal links and thermal shielding

At low temperature, electronic noise and thermal broadening effect are suppressed dramatically, enabling the observation of many novel physical phenomena. Therefore, it is of vital importance for the system to achieve temperatures as low as possible. Originally, a continuous flow cryostat was used to cool down the sample, and the lowest temperature attainable was about 130 K using  $\text{LN}_2$  as cooling media. LHe is used to further cool down the system. However, due to the high cryogen consumption rate and lack of efficient thermal links and thermal shielding, the lowest attainable temperature was never satisfactory. In the original thermal design, only the sample stage was thermally anchored to the cold finger through a copper braid, while all the other parts of the system, including all the probes, stayed at room temperature all the time. So a great temperature gradient was established between the sample and the probes, degrading the stability and reliability of the system when running at reduced temperature.<sup>18,27</sup> Moreover, the exposure of the sample to room-temperature surroundings further deteriorated the performance of the system at lower temperatures.

The continuous-flow cryostat consists of a cold finger and a surrounding radiation shield tube as shown in Fig. 2(a). This part is located directly below the XY coarse motion actuator for the sample stage as shown in Fig. 2(b). The radiation shield is also cooled by the exhaust gas. In our new design, two arc-shaped pieces tightly hooped onto the outer surface of the radiation shield, along with the cold finger, act as cold sources to cool down probes, sample stage, and thermal shields,

separately. To facilitate brazing the copper braids, some holes and grooves were machined on the cold finger and the arc-shaped pieces.

The sample stage is enclosed by two layers of specially designed thermal shields (inner shield and outer shield) as shown in Fig. 2(b). Each shield has a removable door with a handle on it. When changing probes or sample, the two doors can be removed and put aside in turns by the wobble stick. To enable the positioning of sample and probes by the newly equipped optical microscope, two concentric holes (8 mm in diameter) were drilled in the top of the thermal shields. Connectors C1 and C2 are thermally connected to the inner shield and to the cold finger via several brazed copper braids. Furthermore, connectors C3 and C4 are tightly fixed to the outer shield and connected to the arc-shaped pieces via several brazed copper braids. Four sapphire disks are sandwiched between the inner shield and sample stage tightly, which ensures good thermal conduction and electrical isolation (not shown). The inner shield is isolated electronically and thermally from the outer shield by several alumina washers stacked between the bottom parts of each shield.

A home-made probe holder, composed of a mini scanner tube, a newly designed cantilever, a sapphire plate, and a 10-pin electrode, is placed on the big scanner tube (from the commercial design) as shown in Fig. 2(c). The mechanical design will be introduced in detail in Sec. III C. A piece of sapphire is glued onto the top of the big scanner tube by Epo-Tek H74F non-conductive epoxy [Fig. 2(d)]. Ten spring contacts (five on either side) made of beryllium copper plated with gold and a T-shaped connector C5 are fixed by SS nuts and bolts isolated electronically by Teflon sheets. The corresponding electrodes are fixed on the upper sapphire by screws and small Teflon plates. The ten spring contacts pushing the ten corresponding electrodes in the new probe holder prevent the vibrations of the newly designed probe holder in the XY plane. Moreover, the matching of two centering rods in the lower sapphire and two centering holes in the upper one further ensures the mechanical stability of the new probe holder. Originally, the old probe holder was magnetically clamped on top of the big scanner tube. In our design, a magnetic clamping mechanism is also introduced. The embedded magnets together with 10 spring contacts ensure both good mechanical stability and reliable thermal/electrical contact. The new probe holder together with the lower sapphire plate is cooled down through the T-shaped connector C5 that is thermally linked to the arc-shaped pieces. These parts on thermal paths mentioned above, including the shields, cold finger, arc-shaped pieces, copper braids, and these connectors, are all made of OFHC copper plated with gold.

Once the new probes are attached to the base of the scanning unit, the coarse motion of the new cantilever will be restricted within the side window of the shields [see Fig. 2(b)]. The lateral coarse motion range of the cantilever within the frame is  $\pm 3.5 \text{ mm}$  in the X direction and  $\pm 5 \text{ mm}$  in the Y direction. In order to exchange the probes and the sample, the doors of the two layers of shields with handles need to be removed in turns by the wobble stick as shown in Figs. 2(e) and 2(f). The handle on the new cantilever can be gripped by the wobble stick for attaching or detaching the new probe holder

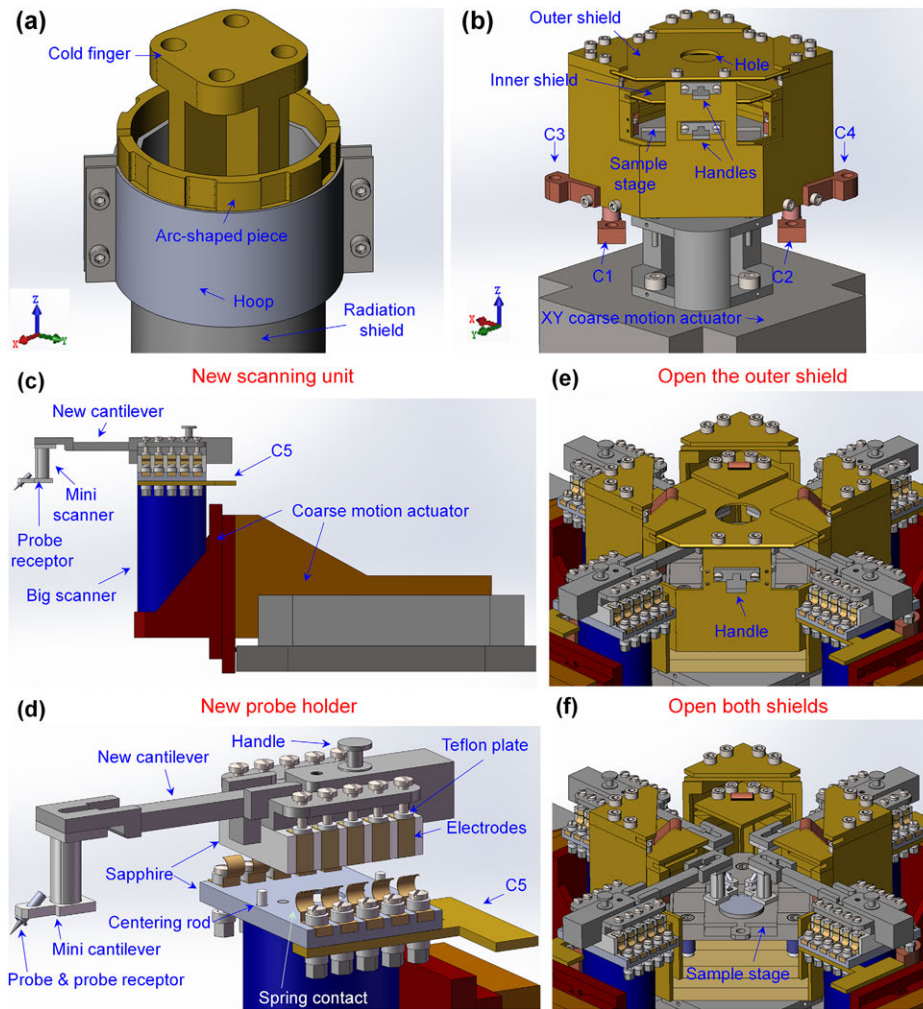


FIG. 2. Thermal design and new scanning unit for the four-probe STM system. (a) Sketch of the upgrading scheme for the continuous-flow cryostat. (b) Diagram showing the inner and outer shields surrounding the sample stage. (c) The new scanning unit with new probe holder clamped on the top of the big scanner. The big scanner is supported by the XYZ coarse motion actuator. (d) Close view of the new probe holder. The spring contact ensures a good electrical contact and a reliable thermal and mechanical connection. (e) Diagram showing the outer shield is open. (f) Schematic showing both shields are open.

[Fig. 2(d)]. Once the probes or samples are replaced by new ones, the doors of thermal shields can be closed by the wobble stick again.

### C. Mechanical design

To ensure the stability of the tunneling junction during STM imaging, a higher mechanical resonance frequency, i.e., a rigid body, is desired.<sup>56</sup> By virtue of the inherent structural damping of a rigid construction, vibrations can be dissipated by hysteresis loss.<sup>52</sup> However, the original cantilever was approximately 30 mm long. This lathy structure was easily disturbed by external vibration, resulting in a noisy tunneling junction. Before the modification, atomic resolution was hardly obtained.

Our mechanical design is shown in Figs. 2(c) and 2(d). As mentioned earlier, the original scanning unit included an XYZ coarse motion actuator, a big scanner tube, and a probe holder with a long cantilever. In our new scanning unit, the XYZ coarse motion actuator and the original scanner tube (big scanner) were kept, while the probe holder was replaced. A close view of the new probe holder is shown in Fig. 2(d). The mini scanner is capable of generating displacement in X, Y, and Z directions and implementing STM scanning alone. The resonance frequency (Hz) of the mini piezo tube can be

estimated by

$$f_r = 1.08 \times 10^5 [(r_o^2 + r_i^2)^{1/2} / l^2], \quad (2)$$

where  $r_i$  and  $r_o$  represent the radius of the inner wall and outer wall, respectively, and  $l$  represents the length of the tube in cm.<sup>52</sup> According to Eq. (2), the resonance frequency of the mini piezo tube ( $r_i = 0.159$  cm,  $r_o = 0.109$  cm, and  $l = 0.8$  cm) is 32.5 kHz, which is far above the cutoff frequency in the feedback loop controller (1.3 kHz, cutoff frequency of our home-made preamplifier) for the tunneling gap.<sup>1</sup> Thus the effect of the internal vibrations of scanners during scanning can be eliminated.<sup>1</sup>

The new cantilevers driven by the coarse motion actuator can move in three directions. However, the motion of the new cantilever, which extends into the thermal shields through windows, is limited within the windows frame of the shields. As a result, the design of the new cantilever is a compromise between coarse movement range and rigidity. The mini scanner is glued beneath the front of the new cantilever. The axis of the mini scanner tube is vertical to the sample surface, while the probe mounted in the spring loaded receptor is oriented at  $\sim 45^\circ$  relative to the normal of the sample surface. The probe receptor and the bottom of the mini scanner tube are all glued together via non-conductive epoxy to a mini cantilever made of a machinable ceramic material.

We simulated the oscillatory behavior of the newly designed cantilevers by the finite element method (FEM). The simulated oscillation images of the new cantilever and the mini cantilever at the first two mechanical eigenmodes are displayed in Figs. 3(a)–3(d). The color bar shows the normalized relative displacement (a.u.) from the static state. The displacement is scaled up so as to make the oscillatory behavior observable. The new cantilever will bend mainly in the Z plane at mode 1 while it will vibrate in the XY plane at mode 2, which is explicitly shown in Figs. 3(a) and 3(b). The oscillatory behavior of the mini cantilever with the mini scanner and the probe receptor resembles that of the new cantilever, while the oscillation at mode 2 mainly focuses on the probe [Figs. 3(c) and 3(d)]. The resonance frequencies of the newly designed cantilevers and the original cantilever are summarized in Fig. 3(e). Unlike the results in our scheme, the original cantilever oscillates in

the XY plane at its first eigenmode (black bar on the left) while it vibrates in the Z plane at the second eigenmode (red bar on the right). The first two resonance frequencies of the original cantilever are 2642.7 and 2655.7 Hz, and those of the new cantilever are in the same level: 2236.7 and 3323.8 Hz. As for the mini scanner, its first two resonance frequencies are 38 549 and 81 714 Hz, more than an order of magnitude higher. Although the simulated dynamics results show that the resonance frequency of the new cantilever in the z direction is decreased somewhat compared with that of the original cantilever, it is desirable to point out that the new cantilever will actually be in static state and the mini cantilever possesses much higher resonance frequencies when scanning with the mini scanner. Based on the simulated dynamics results, we can conclude that the new design possesses better mechanical stability. Additionally, in order to further improve the mechanical stability, the center of gravity of the new probe holder is designed to be in the axis of the big scanner tube.

After upgrading, there are eight scanners in total, including four old (big) ones and four new (mini) ones. The scanning ranges of the old and new scanner are  $5\ \mu\text{m} \times 5\ \mu\text{m} \times 2\ \mu\text{m}$  and  $400\ \text{nm} \times 400\ \text{nm} \times 200\ \text{nm}$  in XYZ directions at room temperature, respectively. This two-scanner structure, combining a big scanner with a mini scanner together, has a unique advantage: larger scanning range and higher piezo tube sensitivity/spatial resolution can be achieved simultaneously. However, driving eight piezo tubes simultaneously is beyond the capability of regular SPM controllers. We are now developing a time-shared control unit that has many features specially designed for the 4-P STM, including the capability of driving eight piezo tubes by one SPM controller. A detailed description of the time-shared control unit will be reported later. Integration of AFM based on the qPlus technique is also in progress.

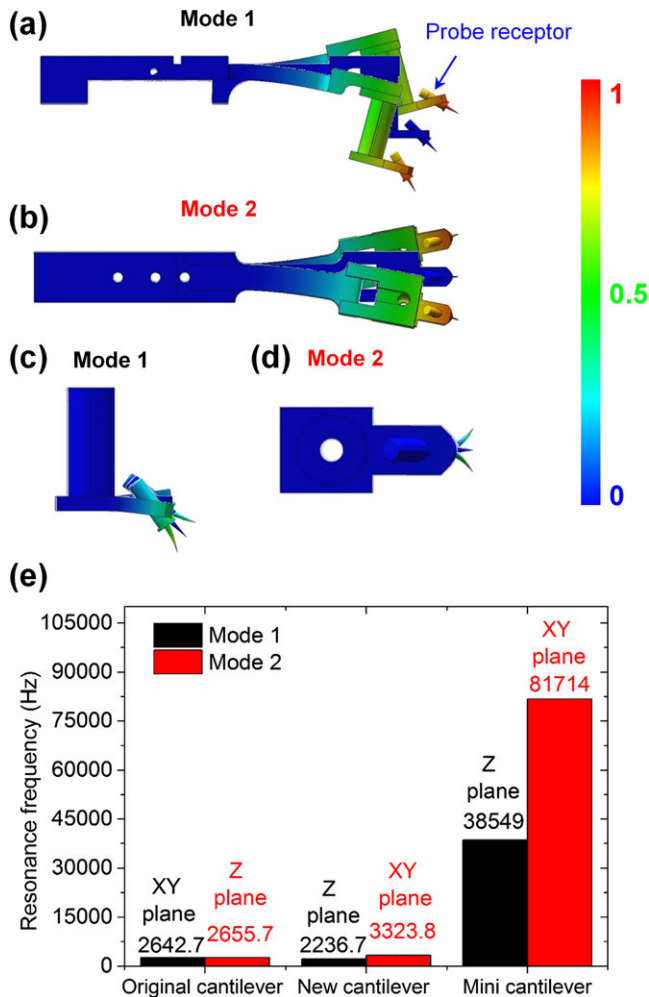


FIG. 3. Oscillatory behavior analysis of cantilevers by the finite element method. [(a) and (b)] Simulated images of a new cantilever with the mini scanner oscillating at the first two resonance frequencies, denoted as mode 1 and mode 2, respectively. The new cantilever mainly oscillates in the Z plane at mode 1 and in the XY plane at mode 2. The color bar shows the normalized relative displacement (a.u.) from the static condition. The displacement is exaggerated so as to make the variation clear. [(c) and (d)] Simulated oscillation images for mini cantilever with the mini scanner and the probe receptor. The results follow the same oscillation behavior as the new cantilever in the two eigenmodes. (e) Summary of resonance frequency and the main oscillating plane for the original cantilever, new cantilever, and mini cantilever.

#### D. Replacement of SEM with OM

After upgrading the damping system, the SS plate holding all the scanning units and sample stage is no longer at a fixed position. In addition, 24 SmCo magnets around the stage have been embedded, which would change the path of the electrons emitted by the SEM gun and degrade the imaging capability of the SEM. Therefore, we replaced the SEM with an OM with a tunable working distance ranging from 15 to 35 cm. Despite lower resolution ( $1.1\ \mu\text{m}$ ) compared to that of the SEM ( $20\ \text{nm}$ ), OM is user-friendly and more time-effective to position the probes and samples with the help of a CCD camera. In addition, the illuminating light is non-destructive to samples, especially for single-layer 2D materials, unlike the electrons emitted from the SEM.

Obviously, there is a gap between the practical resolution of the OM ( $1.1\ \mu\text{m}$ ) and the lateral scanning range of the new mini scanner ( $400\ \text{nm} \times 400\ \text{nm}$ ). This can be solved by the two-scanner mechanism. Furthermore, we are developing a time-shared control unit to address this issue. Due to the overlapping of the scanning range of the big scanner ( $5\ \mu\text{m} \times 5\ \mu\text{m}$ ) and the resolution of OM ( $1.1\ \mu\text{m}$ ), we can perform a rough STM positioning by the big scanner to reach the target

structures with the aid of the OM. After that, the connections of the STM control unit are switched to the mini scanner by the time-shared control unit while keeping the voltages applied on the bigger scanner unchanged, and then a more precise scanning can be carried out. In this way, no positioning gap is present.

#### IV. PERFORMANCE

To demonstrate the performance of the upgraded 4-P STM system, we carried out spectral density (SD) measurements of the tunneling current and the Z-height signal vs frequency, STM imaging, cooling cycle testing, and four-point electrical transport measurements.

##### A. Spectral density measurements

The spectral density (SD) of the tunneling current and Z-height signals directly reflects the stability of probe-sample junction.<sup>57</sup> We have carried out SD measurements of the tunneling current and the Z-height signal vs frequency on the upgraded system at room temperature. Figures 4(a) and 4(b) show the SD of the tunneling current as functions of frequency ranging from 0 to 100 Hz, and from 0 to 3 kHz, respectively. When the probe is retracted (out of tunneling), the SD measurement of tunnel current reveals the baseline of noise [black curves in Figs. 4(a) and 4(b)], which may originate from all noise sources including cables, amplifiers, interference effect, ground loops, microphonics, and so on.<sup>57</sup> The noise baseline of our amplifier is between 0.1 and 10 fA/Hz<sup>1/2</sup>, more than one order lower than 100 fA/Hz<sup>1/2</sup>, indicating a quite low level.<sup>57</sup> While there are peaks at 50 Hz and higher harmonics from the pickup of power line noise when the probe is retracted [black curves in Figs. 4(a) and 4(b)], their peak values are all below 10 fA/Hz<sup>1/2</sup>, which will not bring observable noise

during scanning or in the STS mode (constant height mode). When the probe is engaged without feedback (feedback loop open), the tunnel current is sensitive to any changes, such as fluctuations of the probe-sample distance, and reaches a much higher level [blue curves in Figs. 4(a) and 4(b)]. However, their peak values are only 10 fA/Hz<sup>1/2</sup> at 100 Hz, which corresponds to quite small displacement amplitudes,<sup>57</sup> suggesting a stable tunnel junction. When the feedback loop is closed, additional noise coming from the tunneling current and the whole feedback loop is picked up,<sup>57</sup> as shown in red curves in Figs. 4(a) and 4(b). The peak features remain as in the case for “feedback loop open” but the noise level is reduced by 10–100 times especially at frequencies lower than 20 Hz, as shown in Fig. 4(a). This reduction is due to the feedback loop which continuously moves the probe to keep the current constant. It is worth mentioning that the peaks at about 2.7 Hz correspond to the resonance frequency of the suspension springs, as indicated by a black arrow in Fig. 4(a). As for frequencies higher than 100 Hz, the curve for “feedback loop open” almost coincides with that for “feedback loop closed” as shown in Fig. 4(b). This further verifies the low-noise level and stability of the tunneling junction. Figures 4(c) and 4(d) reveal the SD of the Z-height signals with low frequencies below 100 Hz and high frequencies up to 3 kHz, respectively. When the feedback loop is open, the HV applied to the Z electrode of the scanner is kept constant, so SD shows no noise features [blue curves in Figs. 4(c) and 4(d)]. When the feedback loop is closed, the noise baseline jumps to a much higher noise level [red curves in Figs. 4(c) and 4(d)]. The Z-height signals share the same peak features as the current signals. These peak values are below 1 pm/Hz<sup>1/2</sup> despite the ones at frequencies below 6 Hz, and at 100 Hz the peak value approaches 50 fm/Hz<sup>1/2</sup>, indicating good performance of the system.<sup>57</sup> Since the resonance frequency of the loaded springs is 2.73 Hz, a peak at ~2.7 Hz is also observed in Fig. 4(c).

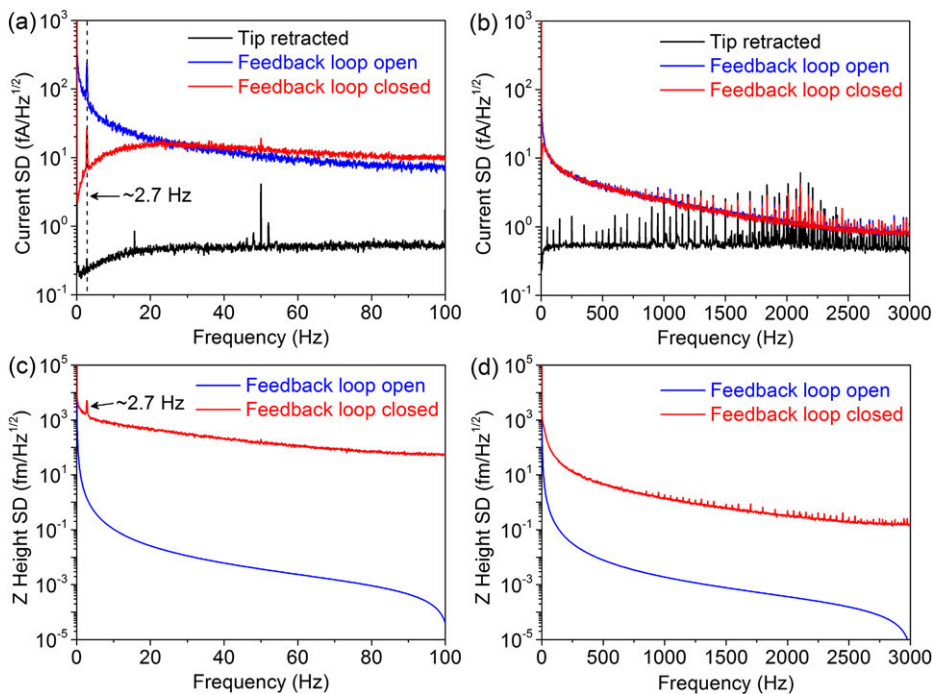


FIG. 4. Characterization of the isolation performance by the spectral density (SD) of the tunneling current and Z-height signals with feedback loop open (blue), feedback loop closed (red), and tip retracted (black), respectively. SD of the current noise as functions of frequency ranging from DC to 100 Hz (a) and from DC to 3 kHz (b). SD of the Z-height signal vs frequency ranging from DC to 100 Hz (c) and from DC to 3 kHz (d). The peaks at 2.73 Hz pointed by black arrows in (a) and (c) are caused by the resonance frequency of the suspension springs holding the STM stage. The peak at 50 Hz and its harmonics are clearly observed due to the pickup of the line frequency in the electrical cables. All these measurements were performed on an HOPG sample at room temperature with a chemically etched W tip. All data are collected from the combination of the home-made preamplifier and a MATRIX controller. Tunnel conditions: tunneling current setpoint 100 pA, sample bias 2.0 V.

## B. STM imaging

Old STM images taken by this commercial instrument can be found in Ref. 25, and the quality is far from satisfactory. As previously mentioned, a new scanner and probe holder are designed to improve the imaging capability of the system. An optical micrograph of the new scanner and probe holder is shown in Fig. 5(a). Originally, all signals are transmitted by bare twisted-pair wires inside the chamber. After upgrading, the tunneling current signals are transmitted via coaxial cables from the probe receptor all the way to the preamplifiers outside the chamber. The shielding is connected to low impedance sources which follow the same potential as the inner wire (biased or in virtual ground) to minimize the leak current. Twisted-pair wires with grounded shielding are used to apply driving voltages to scanners from the piezo tube electrodes to the electronic feedthroughs.

An HOPG sample cleaned by cleaving the contaminated surface layers by a piece of tape was used to test the STM

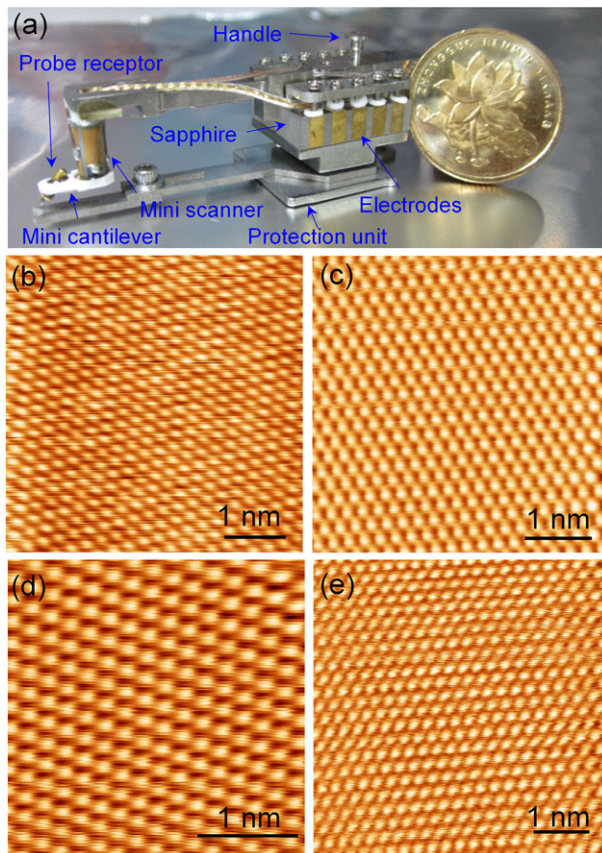


FIG. 5. Photograph of the newly designed probe holder and STM images obtained by the new scanners. (a) General view of the new probe holder. The probe in front of the piezo tube is projecting under  $\sim 45^\circ$  onto the sample surface. The protection unit can prevent the probe and fragile piezo scanner from being broken during transfer from place to place in the chamber. A fifty-cent coin is put in order to give an intuitive concept of the dimension of the new probe holder. (b) Atomically resolved STM image in air at room temperature. (c) STM image with atomic resolution in UHV at room temperature. (d) Atomic-resolution STM image in UHV at 190 K. (e) Atomically resolved STM image in UHV at 110 K. These STM height images are obtained on HOPG by the new scanner shown in (a). Electrochemically etched W probes are used during the scanning processes. Hexagonal structures are clearly resolved. Scanning parameters: (b)  $I_t = 600$  pA and  $V_{\text{sample}} = -400$  mV. (c)–(e)  $I_t = 450$  pA and  $V_{\text{sample}} = -450$  mV.

capability of the mini scanner. Figures 5(b) and 5(c) show atomically resolved images of HOPG surface taken in air and UHV conditions, respectively, wherein hexagonal structures on the HOPG surface are clearly resolved, confirming the system's atomic resolution imaging capability at room temperature. Figures 5(d) and 5(e) show atomically resolved STM images of HOPG surface obtained in UHV conditions at 190 K and 110 K, respectively, in which hexagonal lattices are also clearly resolved. All the STM images are raw data without any processing. These tests are all carried out in the constant current mode by using chemically etched W probes. Atomic resolution images can either be achieved by SCALA controller or MATRIX (OMICRON) controller with the commercial preamplifier or a home-made preamplifier.

The lateral drifts in the STM experiments are also estimated by continuous scanning in a  $200 \text{ nm} \times 200 \text{ nm}$  range on HOPG. The lateral drift at room temperature is about 24 nm/h, while the drifts at 190 K and 110 K are  $\sim 28$  nm/h and  $\sim 41$  nm/h, respectively. Although the thermal broadening effect could be suppressed at lower temperature, the drift in our case is increasing with decreasing sample temperature. This can be attributed to the increasing temperature gradients between the probes and the sample.<sup>58</sup> In other words, the higher temperature gradients are presented between the probes and the sample, the larger thermal drifts are shown.<sup>58</sup> At room temperature, there is no obvious temperature gradient between the probes and the sample. At reduced temperature, the temperature gradient between the probes and the sample is  $\sim 45$  K when the sample is kept at 190 K and the gradient is  $\sim 108$  K when the sample is kept at 110 K [Fig. 6(c)]. Therefore, bigger thermal drift measured at lower temperature is correlated to the increasing temperature gradient. This variation is also reflected in the atomic images: the distortion of lattices due to the thermal drift shown in Fig. 5(e) is more obvious than that shown in Figs. 5(c) and 5(d).

## C. Thermal testing

As previously mentioned, a UHV compatible continuous-flow cryostat is fitted to the commercial 4-P STM system for performing measurements at reduced temperatures. The lowest temperature ever obtained was 130 K when pumping with  $\text{LN}_2$  but no record is available for testing with LHe. For the renewed system, the cooling curves by pumping  $\text{LN}_2$  and LHe can be seen in Figs. 6(a) and 6(b), respectively. The blue solid line depicts the cooling curves of the sample stage measured by a Pt 100 resistor, while the red solid line represents the temperature of cold finger measured by a Si diode. The temperature at the cold finger, which can be tuned by the valve in the transfer tube connecting the Dewar and the cryostat, may fluctuate before stabilizing. As can be seen in Fig. 6(a), it takes approximately 2.5 h for the sample stage to reach temperature as low as 95.9 K, indicated by a black dashed line, when pumping with  $\text{LN}_2$ . For the case with LHe, in Fig. 6(b), the lowest temperature reached by the sample stage was 44.5 K, after one and a half hours cooling. These results verify that the cooling performance is indeed improved by our modification in comparison with the commercial design.



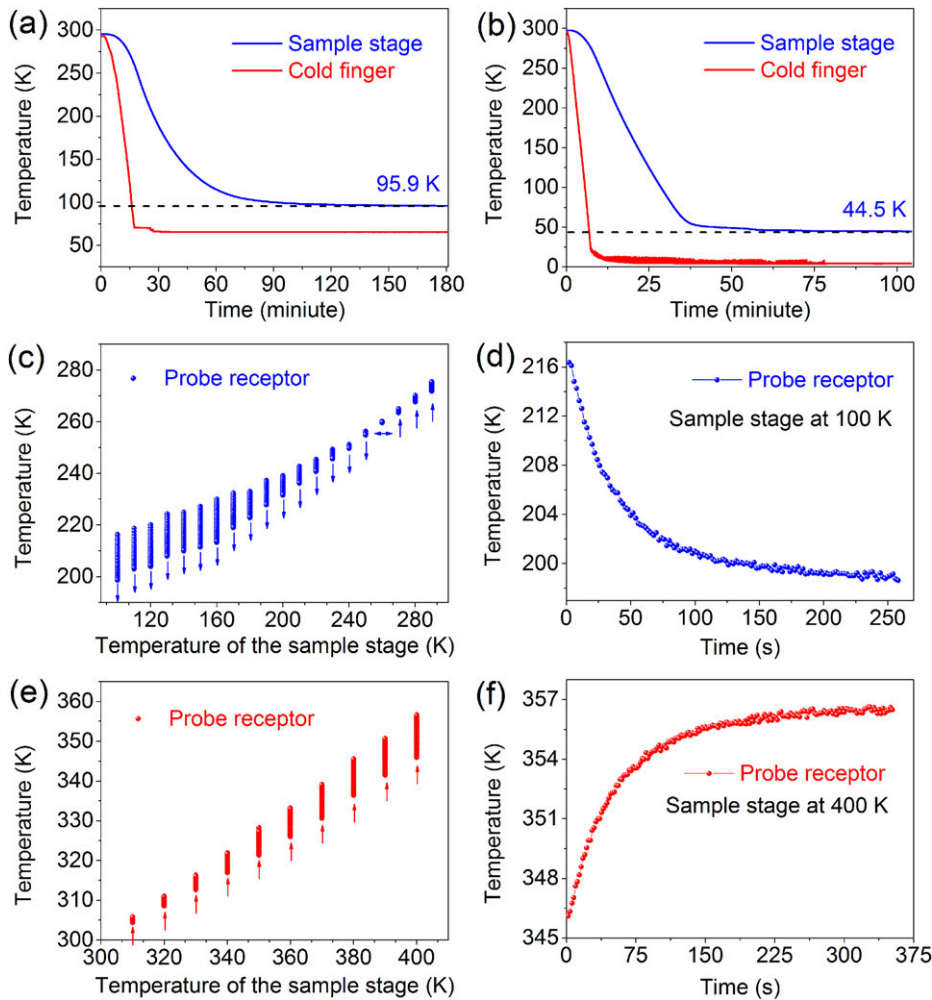


FIG. 6. Thermal testing of our thermal design. Cryostat cooling curves with LN<sub>2</sub> (a) and LHe (b). The blue solid line shows the cooling curve of the sample stage while the red solid curve is for the cold finger. The temperature at the sample stage could be reduced as low as 95.9 K by LN<sub>2</sub>, as indicated by the black dashed line. Cooled by LHe, the lowest temperature of the sample stage is 44.5 K. The temperature at the cold finger can be tuned by the valve in the transfer tube connecting the Dewar and the cryostat. (c) Temperature of the probe receptor with sample stage below room temperature. The temperature of the sample stage is increased step by step with the help of counter-heating. Tracking of the temperature is starting once the probes contact the sample stage to almost thermal-equilibrium state. The upward arrows indicate the temperature going up with increasing time and the downward arrows show the temperature decreasing as time passes. (d) Temperature of the tip receptor as functions of time when the sample stage is kept at 100 K. (e) Temperature of the probe receptor with sample stage above room temperature. In this case, the cooling of the cold finger by continuous flow is not needed. (f) Temperature of the probe receptor vs time when the sample stage, which is maintained at 400 K.

Since the probes are cooled down via thermal links to the cold arc-shaped pieces, we also measured the temperature in the probe receptor by a T-type thermal couple. Figure 6(c) shows the temperature variations of the probe receptor as functions of sample stage temperature. The cold finger is kept at the lowest temperature attainable by pumping LN<sub>2</sub> with a stable continuous flow, while the temperature of the sample stage is increased step by step with the help of a resistive counter-heating element. The blue arrows in Fig. 6(c) indicate variations of temperature at the probe receptor once the probe contacts the sample to the nearly thermal-equilibrium state. The upward arrows indicate the probe temperature going up with increasing time, while the downward arrows show the temperature decreasing as time progresses. During the counter-heating process, the probe receptor temperature is also elevated. When the temperature of the sample stage reaches 260 K, there is no obvious temperature gradient between the probe receptor and the sample stage. Figure 6(d) reveals the temperature of the probe receptor as functions of time after direct contact with the sample, which is kept at 100 K. It takes several minutes for the probe receptor temperature to reach the near equilibrium state ( $\sim 198$  K) from its initial temperature of 217 K before direct contact.

For the transport measurement above room temperature, the cooling of the cold finger by continuous flow is not needed.

Figure 6(e) shows the temperature variations of the probe receptor heated from room temperature. During the heating process, both the temperature of the probe receptor and the sample stage increase, as indicated by the red arrows, and in addition, the temperature gradient is enhanced. Figure 6(f) reveals the temperature measured at the probe receptor vs time after direct contact with the sample, which is maintained at 400 K. It takes approximately six minutes for the probe receptor to reach the near-equilibrium state ( $\sim 357$  K) from the original temperature ( $\sim 346$  K).

In real low-temperature 4-P STM systems,<sup>26,27</sup> the whole STM stage is surrounded by thermal shielding with only small holes for observation. Furthermore, a LHe Dewar is equipped to cool the whole STM stage and the thermal shielding, and thus the probes and the sample stage are in the thermal equilibrium state. However, in our design, the new scanners are only partially enclosed in the thermal shield. As a result, the probes are far from being in thermal equilibrium with the sample.

#### D. Electrical transport measurement

In this section, we demonstrated the transport measurement capability of our 4-P STM by measuring the conductivity of a graphene monolayer on an SiO<sub>2</sub>/Si substrate. Graphene flakes were grown on a copper foil by CVD<sup>59</sup> and then

transferred onto the  $\text{SiO}_2/\text{Si}$  substrate. The domain size can be as large as several millimeters.

The technique for STM probes to approach materials on conducting substrates is quite easy in the four-point conductivity measurement.<sup>27,34,39</sup> As for the conducting material on dielectric substrate, a good point contact can be ensured by judging the contrast in SEM images<sup>30</sup> or by measuring the capacitance between the probes and the sample<sup>60</sup> or using a quadruple-scanning-probe force microscope.<sup>29,61</sup> With regard to our instrument and the tested sample (graphene on  $\text{SiO}_2/\text{Si}$ ), the positioning and approaching procedures are explained as follows:

- (1) For rough engagement, the probes approach the graphene flake with the aid of the OM as elucidated schematically in Fig. 7(a). The virtual image of the probes reflected by the sample surface can serve as an indicator of the distance between probes and sample. The probes can be arranged either in a square configuration or collinear configuration. Furthermore, anisotropic conductivity can be measured by rotating the arrangement relative to the sample surface.<sup>31,41</sup>
- (2) The capacitance between the gate electrode (highly doped Si) and probe 1, for example, is used as the feedback signal for the probe automatically approaching. As long as a good point contact is established, the capacitance will jump to a higher value than the initial wire capacitance. For instance, if the graphene flake size is  $200\ \mu\text{m} \times 200\ \mu\text{m}$  and the dielectric layer of  $\text{SiO}_2$  is

300 nm thick, additional 4.6 pF capacitance can be detected when the probe contacts the graphene flake. Once the automatic approach is done, the scanner will hold the probe in position.

- (3) As for other probes, the approaching procedure can be completed either in the same way as the first probe or by engaging the probe via the traditional STM tip engagement process since the graphene flake could be grounded or biased via the first probe.
- (4) Once all the point contacts are established, all the probes will be switched to the corresponding preamplifiers of a Keithley 4200 test system and the gate is connected to a Keithley 6430 source meter. The probes can be further engaged toward the sample surface by tuning the scanner z-offset voltage for good contacts. Figure 7(b) shows the four gold probes contacting the graphene sample are arranged in a quasi-square configuration with a side length of about  $100\ \mu\text{m}$ . “I1\_V23” is defined for the case that probe 1 injects the current to the sample while probe 4 is grounded, and, at the same time, probe 2 and probe 3 are used to measure the potential voltage. The “I2\_V34” setup can be understood in the same manner. The four probes lie nearly in the middle of the graphene flake. The arrows show the main current directions of each setup. Figure 7(c) shows the sheet resistance of the graphene flake as functions of back gate voltage bias in the “I1\_V23” (black triangles) and “I2\_V34” (red circles) setup. The experiments were carried out in UHV conditions at room temperature. The sheet resistance is

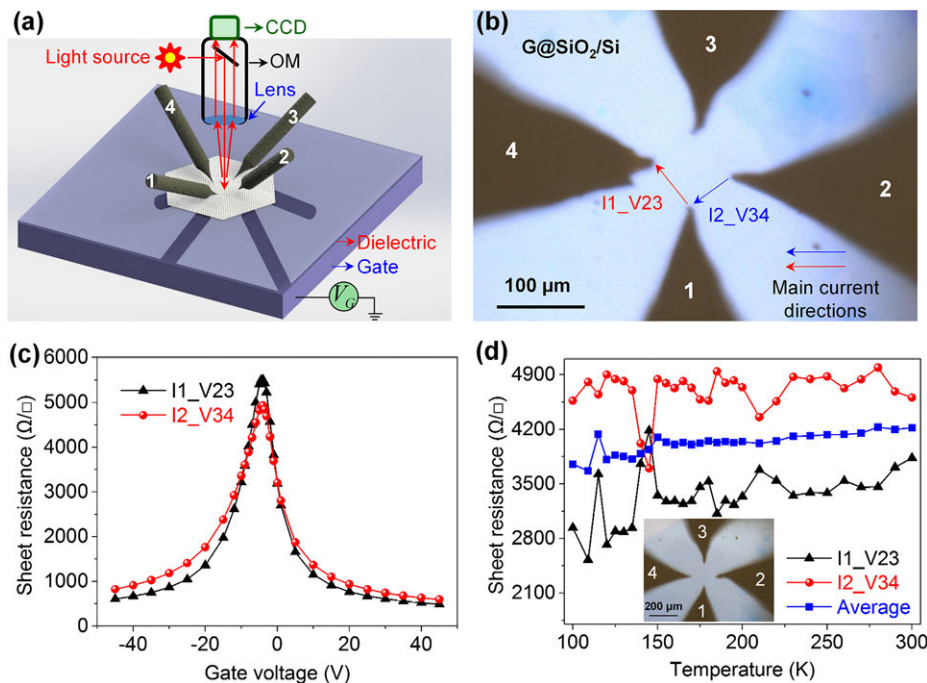


FIG. 7. Four-point transport measurement on graphene@Si/SiO<sub>2</sub>. (a) Experimental setup of electrical transport measurement by 4-P STM. With the aid of real-time OM observation and the capacitance tracking between the probes and gate, the four probes can gently contact the sample on the dielectric substrate SiO<sub>2</sub>/Si. The four probes are connected to a Keithley 4200 instrument while the gate voltage is applied by a Keithley 6430 source meter. (b) Optical micrograph taken by the OM with a CCD camera, which shows the four gold probes contacting the graphene on SiO<sub>2</sub>/Si (G@SiO<sub>2</sub>/Si) in a quasi-square configuration. Setups, I1\_V23 and I2\_V34, are used in the transport measurement. The arrows indicate the main current directions during the measurement. The scale bar is  $100\ \mu\text{m}$ . (c) Measured sheet resistance of G@SiO<sub>2</sub>/Si with tunable gate voltage at room temperature. (d) Sheet resistance of G@SiO<sub>2</sub>/Si as a function of temperature ranging from 100 K to 300 K. The inset figure shows the photograph of the four probes during the measurement. The scale bar is  $200\ \mu\text{m}$ .

extracted by linearly fitting the current versus voltage curve, and a geometry factor of  $2\pi/\ln 2$  is multiplied.<sup>62</sup> Moreover, we can get the averaging conductance of the graphene flake by the van der Pauw method<sup>63</sup> and further calculate the hole mobility and electron mobility (not shown here).

Figure 7(d) shows the sheet resistance of the graphene flake at reduced temperature (100 K–300 K) with zero gate voltage in the “I1\_V23” (black triangles) and “I2\_V34” (red circles) setup. The averaged sheet resistance (blue squares) is roughly decreasing with reducing the temperature, which is consistent with the previous report.<sup>64</sup>

As for the conducting films on insulating substrate mentioned above, the tunneling current is not applicable in the probe approaching process. Originally, the probes are moved toward to the sample surface with the aid of the SEM until slight bending of probe apex occurs. In addition, the probes and sample always had the unstable contact problems (loose contact or tight contact which leads to the severe bending of the probe apex) due to the mechanical instability of the commercial system. Furthermore, the electron emitted by the SEM could bring damages to the sample. In the upgraded system, capacitance is used as a feedback signal in the probe approaching process. In this way, the probes will cause much less damage to the sample compared with the way of judging probe bending. In addition, the mechanical stability of the instrument has been greatly improved as verified by the much better STM imaging capability. As a result, stable contacts are able to be obtained in a controllable manner after the upgrading.

## V. SUMMARY

We have successfully upgraded a commercial 4-P STM system for improving its performance. We have mainly addressed the following four factors:

- (1) Development of the vibration isolation system.
- (2) Enhancement of cooling capability and measurement reliability.
- (3) Improvement of mechanical rigidity and stability.
- (4) Replacement of SEM with OM.

Spectral density measurements, STM imaging, cryostat cooling cycles, and electrical measurements of graphene on SiO<sub>2</sub>/Si demonstrate the enhanced capability of the upgraded system. The renewed system has greatly broadened research fields compared with the commercial one.

## ACKNOWLEDGMENTS

The authors thank Professor Min Ouyang and Professor Xiao Lin for fruitful discussions. This work is financially supported by the National Key Scientific Instrument and Equipment Development Project of China (No. 2013YQ1203451), the National Natural Science Foundation of China (Grant Nos. 61474141 and 61674170), and the Equipment Development Project of Chinese Academy of Sciences (Grant No. yz201450).

- <sup>1</sup>G. Binnig and H. Rohrer, *Helv. Phys. Acta* **55**, 726 (1982).
- <sup>2</sup>G. Binnig, H. Rohrer, Ch. Gerber, and E. Weibel, *Phys. Rev. Lett.* **49**, 57 (1982).
- <sup>3</sup>G. Binnig, C. F. Quate, and Ch. Gerber, *Phys. Rev. Lett.* **56**, 930 (1986).
- <sup>4</sup>C. A. Bobisch, Ph.D. thesis, University of Duisburg-Essen, 2007.
- <sup>5</sup>A. Bannani, C. A. Bobisch, and R. Möller, *Rev. Sci. Instrum.* **79**, 083704 (2008).
- <sup>6</sup>K. W. Clark, X.-G. Zhang, I. V. Vlassiuk, G. He, R. M. Feenstra, and A.-P. Li, *ACS Nano* **7**, 7956 (2013).
- <sup>7</sup>P. Muralt and D. W. Pohl, *Appl. Phys. Lett.* **48**, 514 (1986).
- <sup>8</sup>B. G. Briner, R. M. Feenstra, T. P. Chin, and J. M. Woodall, *Phys. Rev. B* **54**, R5283 (1996).
- <sup>9</sup>K. W. Clark, X.-G. Zhang, G. Gu, J. Park, G. He, R. M. Feenstra, and A.-P. Li, *Phys. Rev. X* **4**, 011021 (2014).
- <sup>10</sup>C. C. Williams and H. K. Wickramasinghe, *Nature* **344**, 317 (1990).
- <sup>11</sup>J. C. Poler, R. M. Zimmermann, and E. C. Cox, *Langmuir* **11**, 2689 (1995).
- <sup>12</sup>J. Park, G. He, R. M. Feenstra, and A.-P. Li, *Nano Lett.* **13**, 3269 (2013).
- <sup>13</sup>R. Wiesendanger, *Rev. Mod. Phys.* **81**, 1495 (2009).
- <sup>14</sup>J. Park, C. Park, M. Yoon, and A.-P. Li, *Nano Lett.* **17**, 292 (2017).
- <sup>15</sup>D. W. Pohl, W. Denk, and M. Lanz, *Appl. Phys. Lett.* **44**, 651 (1984).
- <sup>16</sup>A. Harootunian, E. Betzig, M. Isaacson, and A. Lewis, *Appl. Phys. Lett.* **49**, 674 (1986).
- <sup>17</sup>T. Nakayama, O. Kubo, Y. Shingaya, S. Higuchi, T. Hasegawa, C.-S. Jiang, T. Okuda, Y. Kuwahara, K. Takami, and M. Aono, *Adv. Mater.* **24**, 1675 (2012).
- <sup>18</sup>A.-P. Li, K. W. Clark, X.-G. Zhang, and A. P. Baddorf, *Adv. Funct. Mater.* **23**, 2509 (2013).
- <sup>19</sup>H. Grube, B. C. Harrison, J. Jia, and J. J. Boland, *Rev. Sci. Instrum.* **72**, 4388 (2001).
- <sup>20</sup>H. Watanabe, C. Manabe, T. Shigematsu, and M. Shimizu, *Appl. Phys. Lett.* **78**, 2928 (2001).
- <sup>21</sup>E. Tsunemi, K. Kobayashi, K. Matsushige, and H. Yamada, *Rev. Sci. Instrum.* **82**, 033708 (2011).
- <sup>22</sup>H. Watanabe, C. Manabe, T. Shigematsu, K. Shimotani, and M. Shimizu, *Appl. Phys. Lett.* **79**, 2462 (2001).
- <sup>23</sup>M. Salomons, B. V. C. Martins, J. Zikovsky, and R. A. Wolkow, *Rev. Sci. Instrum.* **85**, 045126 (2014).
- <sup>24</sup>I. Shiraki, F. Tanabe, R. Hobara, T. Nagao, and S. Hasegawa, *Surf. Sci.* **493**, 633 (2001).
- <sup>25</sup>X. Lin, X. B. He, J. L. Lu, L. Gao, Q. Huan, D. X. Shi, and H. J. Gao, *Chin. Phys. Lett.* **14**, 1536 (2005).
- <sup>26</sup>R. Hobara, N. Nagamura, S. Hasegawa, I. Matsuda, Y. Yamamoto, Y. Miyatake, and T. Nagamura, *Rev. Sci. Instrum.* **78**, 053705 (2007).
- <sup>27</sup>T.-H. Kim, Z. Wang, J. F. Wendelken, H. H. Weitering, W. Li, and A.-P. Li, *Rev. Sci. Instrum.* **78**, 123701 (2007).
- <sup>28</sup>S. Higuchi, H. Kuramochi, O. Laurent, T. Komatsubara, S. Machida, M. Aono, K. Obori, and T. Nakayama, *Rev. Sci. Instrum.* **81**, 073706 (2010).
- <sup>29</sup>S. Higuchi, O. Kubo, H. Kuramochi, M. Aono, and T. Nakayama, *Nanotechnology* **22**, 285205 (2011).
- <sup>30</sup>V. Cherepanov, E. Zubkov, H. Junker, S. Korte, M. Blab, P. Coenen, and B. Voigtländer, *Rev. Sci. Instrum.* **83**, 033707 (2012).
- <sup>31</sup>T. Kanagawa, R. Hobara, I. Matsuda, T. Tanikawa, A. Natori, and S. Hasegawa, *Phys. Rev. Lett.* **91**, 036805 (2003).
- <sup>32</sup>I. Matsuda, C. Liu, T. Hirahara, M. Ueno, T. Tanikawa, T. Kanagawa, R. Hobara, S. Yamazaki, and S. Hasegawa, *Phys. Rev. Lett.* **99**, 146805 (2007).
- <sup>33</sup>S. Yoshimoto, Y. Murata, K. Kubo, K. Tomita, K. Motoyoshi, T. Kimura, H. Okino, R. Hobara, I. Matsuda, S.-i. Honda, M. Katayama, and S. Hasegawa, *Nano Lett.* **7**, 956 (2007).
- <sup>34</sup>O. Guise, H. Marbach, J. T. Yates, Jr., M.-C. Jung, J. Levy, and J. Ahner, *Rev. Sci. Instrum.* **76**, 045107 (2005).
- <sup>35</sup>X. Lin, X. B. He, T. Z. Yang, W. Guo, D. X. Shi, H.-J. Gao, D. D. Ma, S. T. Lee, F. Liu, and X. C. Xie, *Appl. Phys. Lett.* **89**, 043103 (2006).
- <sup>36</sup>Y. Kitaoka, T. Tono, S. Yoshimoto, T. Hirahara, S. Hasegawa, and T. Ohba, *Appl. Phys. Lett.* **95**, 052110 (2009).
- <sup>37</sup>T. Uetake, T. Hirahara, Y. Ueda, N. Nagamura, R. Hobara, and S. Hasegawa, *Phys. Rev. B* **86**, 035325 (2012).
- <sup>38</sup>N. Nagamura, R. Hobara, T. Uetake, T. Hirahara, M. Ogawa, T. Okuda, K. He, P. Moras, P. M. Sheverdyeva, C. Carbone, K. Kobayashi, I. Matsuda, and S. Hasegawa, *Phys. Rev. B* **89**, 125415 (2014).
- <sup>39</sup>P. W. Sutter, J.-I. Flege, and E. A. Sutter, *Nat. Mater.* **7**, 406 (2008).
- <sup>40</sup>H. L. Lu, C. D. Zhang, H. M. Guo, H. J. Gao, M. Liu, J. A. Liu, G. Collins, and C. L. Chen, *ACS Appl. Mater. Interfaces* **2**, 2496 (2010).

- <sup>41</sup>M. K. Yakes, D. Gunlycke, J. L. Tedesco, P. M. Campbell, R. L. Myers-Ward, C. R. Eddy, Jr., D. K. Gaskill, P. E. Sheehan, and A. R. Laracuente, *Nano Lett.* **10**, 1559 (2010).
- <sup>42</sup>M. Liu, Q. Zou, C. R. Ma, G. Collins, S.-B. Mi, C.-L. Jia, H. M. Guo, H. J. Gao, and C. L. Chen, *ACS Appl. Mater. Interfaces* **6**, 8526 (2014).
- <sup>43</sup>Q. Zou, M. Liu, G. Q. Wang, H. L. Lu, T. Z. Yang, H. M. Guo, C. R. Ma, X. Xu, M. H. Zhang, J. C. Jiang, E. I. Meletis, Y. Lin, H. J. Gao, and C. L. Chen, *ACS Appl. Mater. Interfaces* **6**, 6704 (2014).
- <sup>44</sup>J. C. Li, Y. Wang, and D. C. Ba, *Phys. Procedia* **32**, 347 (2012).
- <sup>45</sup>C. Durand, X.-G. Zhang, S. M. Hus, C. Ma, M. A. McGuire, Y. Xu, H. Cao, I. Miotkowski, Y. P. Chen, and A.-P. Li, *Nano Lett.* **16**, 2213 (2016).
- <sup>46</sup>T. Kambe, R. Sakamoto, T. Kusamoto, T. Pal, N. Fukui, K. Hoshiko, T. Shimojima, Z. Wang, T. Hirahara, K. Ishizaka, S. Hasegawa, F. Liu, and H. Nishihara, *J. Am. Chem. Soc.* **136**, 14357 (2014).
- <sup>47</sup>Z. Shi, H. Lu, L. Zhang, R. Yang, Y. Wang, D. Liu, H. Guo, D. Shi, H. Gao, E. Wang, and G. Zhang, *Nano Res.* **5**, 82 (2011).
- <sup>48</sup>S. Just, M. Blab, S. Korte, V. Cherepanov, H. Soltner, and B. Voigtländer, *Phys. Rev. Lett.* **115**, 066801 (2015).
- <sup>49</sup>A. Bannani, C. Bobisch, and R. Möller, *Science* **315**, 1824 (2007).
- <sup>50</sup>C. A. Bobisch, A. Bannani, A. Bernhart, E. Zubkov, B. Weyers, and R. Möller, *J. Phys.: Conf. Ser.* **100**, 052064 (2008).
- <sup>51</sup>M. Gao, Y. Pan, C. Zhang, H. Hu, R. Yang, H. Lu, J. Cai, S. Du, F. Liu, and H.-J. Gao, *Appl. Phys. Lett.* **96**, 053109 (2010).
- <sup>52</sup>Y. Kuk and P. J. Silverman, *Rev. Sci. Instrum.* **60**, 165 (1989).
- <sup>53</sup>A. I. Oliva, M. Aguilar, and V. Sosa, *Meas. Sci. Technol.* **9**, 383 (1998).
- <sup>54</sup>Ch. Gerber, G. Binnig, H. Fuchs, O. Marti, and H. Rohrer, *Rev. Sci. Instrum.* **57**, 221 (1986).
- <sup>55</sup>J. M. Hensley, A. Peters, and S. Chu, *Rev. Sci. Instrum.* **70**, 2735 (1999).
- <sup>56</sup>C. R. Ast, M. Assig, A. Ast, and K. Kern, *Rev. Sci. Instrum.* **79**, 093704 (2008).
- <sup>57</sup>Y. J. Song, A. F. Otte, V. Shvarts, Z. Zhao, Y. Kuk, S. R. Blankenship, A. Band, F. M. Hess, and J. A. Stroschio, *Rev. Sci. Instrum.* **81**, 121101 (2010).
- <sup>58</sup>B. Bhushan, *Nanotribology and Nanomechanics: An Introduction* (Springer Science & Business Media, 2008), p. 183.
- <sup>59</sup>W. Guo, B. Wu, Y. Li, L. Wang, J. Chen, B. Chen, Z. Zhang, L. Peng, S. Wang, and Y. Liu, *ACS Nano* **9**, 5792 (2015).
- <sup>60</sup>G. Li, A. Luican, and E. Y. Andrei, *Rev. Sci. Instrum.* **82**, 073701 (2011).
- <sup>61</sup>S. Higuchi, H. Kuramochi, O. Kubo, S. Masuda, Y. Shingaya, M. Aono, and T. Nakayama, *Rev. Sci. Instrum.* **82**, 043701 (2011).
- <sup>62</sup>I. Miccoli, F. Edler, H. Pfnür, and C. Tegenkamp, *J. Phys.: Condens. Matter* **27**, 223201 (2015).
- <sup>63</sup>L. J. Van der Pauw, *Philips Res. Rep.* **13**, 1 (1958).
- <sup>64</sup>S. Das Sarma, S. Adam, E. H. Hwang, and E. Rossi, *Rev. Mod. Phys.* **83**, 407 (2011).